Colony-like Protocell Superstructures

Chinmay Katke,[#] Esteban Pedrueza-Villalmanzo,[#] Karolina Spustova, Ruslan Ryskulov, C. Nadir Kaplan,* and Irep Gözen*

Read Online

ACCESS | Metrics & More | Article Recommendations | Supporting Information

ABSTRACT: We report the formation, growth, and dynamics of model protocell superstructures on solid surfaces, resembling single cell colonies. These structures, consisting of several layers of lipidic compartments enveloped in a dome-shaped outer lipid bilayer, emerged as a result of spontaneous shape transformation of lipid agglomerates deposited on thin film aluminum surfaces. Collective protocell structures were observed to be mechanically more stable compared to isolated spherical compartments. We show that the model colonies encapsulate DNA and accommodate nonenzymatic, strand displacement DNA reactions. The membrane envelope is able to disassemble and expose individual daughter protocells, which can migrate and attach via nanotethers to distant surface locations, while maintaining their encapsulated contents. Some colonies feature "exocompartments", which spontaneously extend out of the enveloping bilayer, internalize DNA, and merge again with the superstructure. A continuum elastohydrodynamic theory that we developed suggests that a plausible driving force behind subcompartment formation is attractive van der Waals (vdW) interactions between the membrane and surface. The balance between membrane bending and vdW interactions yields a critical length scale of 236 nm, above which the membrane invaginations can form subcompartments. The findings support our hypotheses that in extension of the "lipid world hypothesis", protocells may have existed in the form of colonies, potentially benefiting from the increased mechanical stability provided by a superstructure.

KEYWORDS: protocell, compartmentalization, superstructure, lipid, colony, origin of life, van der Waals
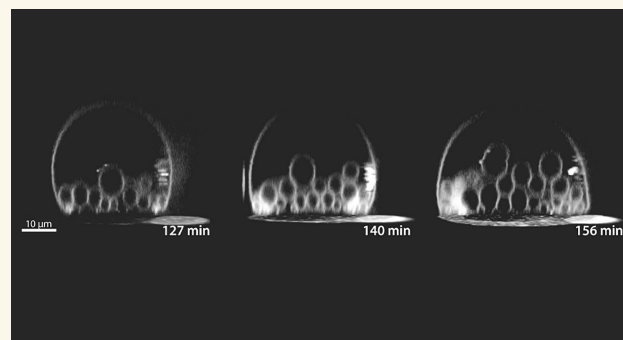
INTRODUCTION

How the first biological cells came into existence on the early Earth is still an unanswered question. Significant research efforts have been directed toward the fabrication and studies of artificial compartments made from prebiotically plausible materials, i.e., the protocells, to program and understand their behavior and recreate the potential steps of development toward life. Since the first living cells are hypothesized to have a bilayer boundary[1] and their modern counterparts also feature an enveloping bilayer, mammalian cell-sized spherical lipid-enveloped compartments, i.e., giant vesicles,[2,3] are prominent among protocell models.

An individual protocell in an aqueous environment would have its membrane directly exposed to the fluid medium around it, subject to a plethora of mechanical, chemical, and physicochemical challenges, such as shear stress due to agitation by currents and convection, osmotic stress, and pH fluctuations. An interesting alternative scenario was proposed to be the collective evolution of protocells, in the form of "vesicle colonies".[4,5] Protocell colonies could have provided mutual benefits such as increased stability under harsh environmental conditions, and protocell communication by facilitating material exchange among the closely spaced compartments within the colony. High mechanical stability[6] and enhanced material transfer would provide an advantage for primitive cells in the light of Darwinian evolution.

Agglomerates of giant unilamellar vesicles have been previously experimentally prepared, e.g., by bringing together initially isolated vesicles using adhesive molecules such as poly-L-arginine,[7] complementary DNA strands,[8] streptavidin−biotin,[8] divalent cations,[9] or oppositely charged biopolymers.[10] Similar structures were formed by directed assembly using instrumental techniques, including acoustical trapping,[11] optical tweezers,[12] and magnetic manipulation.[13] One example of a colony-like vesicular structure under prebiologically plausible conditions was reported, where osmotic shock of vesicles led to shrinkage of a lipid vesicle and formation of
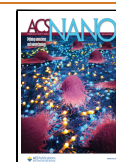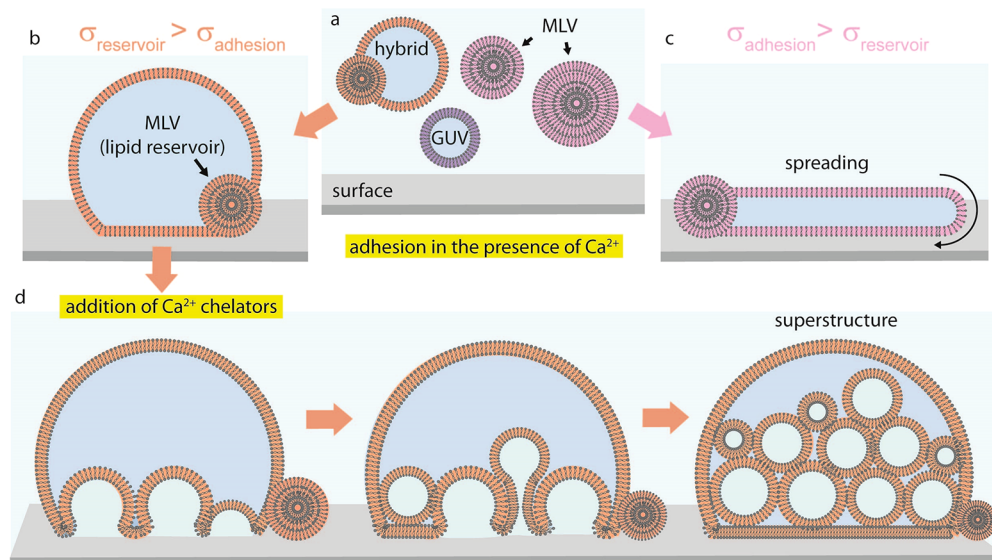
Figure 1. Schematic drawing showing the formation of superstructures. (a) A lipid suspension containing uni- and multilamellar vesicles (MLV) as well as hybrid vesicles comprised of both is deposited onto an aluminum substrate submerged in an aqueous solution containing Ca^{2+} ions. (b) Hybrid compartments adopt a semiadhered, dome-shape morphology when reservoir tension is larger than adhesion energy ($\sigma_{reservoir} > \sigma_{adhesion}$). (c) If $\sigma_{adhesion} > \sigma_{reservoir}$ the MLVs spread on the surface, resulting in formation of a flat giant unilamellar vesicle (FGUV). (d) Exposure to Ca^{2+} chelators leads to removal of Ca^{2+} from the membrane surface interface and results in the formation of superstructures.

inverted daughter vesicles.[14] This transformation is presumably lipid dependent, as vesicles made from certain lipid species did not exhibit this behavior.[14] Most recently, we showed the formation of colony-like model protocells emerging from the molecular lipid films on early Earth minerals and a Martian meteorite.[15]

Here we report the stepwise formation and growth of protocell superstructures containing tens to thousands of membranous compartments, originating from a single onion-shell lipid reservoir. Inside a lipid compartment, several layers of smaller vesicles grow from the surface up, leading to a densely packed pool of compartments of similar shape and size, reminiscent of bacterial colonies. We predicted that the intravesicular compartments can grow from membrane undulations above a critical wavelength of 236 nm when the van der Waals (vdW) interactions are attractive between the solid surface and the membrane closely positioned to it. The formed compartments can then expand and fuse over time. Eventually, the original protocell, which serves as the enveloping layer and boundary for the colony, can disintegrate. We demonstrate that the protocell colonies, either enveloped in a bilayer or directly exposed, are mechanically more robust compared to individual compartments, can encapsulate DNA, and accommodate nonenzymatic DNA strand displacement reactions. Some colonies employ "exocompartments", which spontaneously extend out of the enveloping bilayer, uptake DNA, and fuse again with the colony under redistribution of its DNA content. The DNA-encapsulating colonies can disassemble, exposing individual daughter protocells that migrate and attach to distant surface locations via nanotethers, while preserving their DNA content.

We report that distinctly substructured membrane containers with key features of protocells can autonomously and consistently emanate from lipid sources under conceptually simple, prebiotically relevant conditions. Our findings on the self-driven harvesting of surface free energy from solid surfaces

for shape transformations of membrane assemblies point toward a potential key step in the transition pathway from the nonliving to the living world. We provide evidence that the evolution of organelles in primitive single cellular organisms does not necessarily require living cells as foundation but can occur concomitantly with the self-assembly of single shell membranous structures from lipid material. The assembly route to physically separated, confined volumes in a protocell superstructure that can form colonies of enhanced mechanical stability, encapsulate molecules, and pseudodivide, creates opportunities for prebiotic chemistry to overcome the limitations of "one-pot" syntheses that have thus far been explored. The potential of surface-free energy utilization for sophisticated self-organization processes by prebiotic assemblies has been overlooked in the past, a problem which we have addressed in this work.

RESULTS AND DISCUSSION

Formation of Superstructures. Our experiments start with depositing lipid vesicles onto a solid substrate followed by the spontaneous adhesion of the vesicles onto the surface (Figure 1). The vesicles originate from the same lipid suspension; they are in form of uni- and multilamellar vesicles (MLVs) or adopt a hybrid structure consisting of a unilamellar vesicle attached to an MLV (Figure 1a). MLVs are packed with lipid bilayers which can unfold and act as lipid reservoirs. Depending on the balance between the local adhesion energy ($\sigma_{adhesion}$) and the tension of the lipid reservoir ($\sigma_{reservoir}$) the fate of the lipid compartments follow two pathways. If $\sigma_{reservoir} > \sigma_{adhesion}$, the lipid compartments maintain a semiadhered, dome-shape morphology (Figure 1b). When $\sigma_{adhesion} > \sigma_{reservoir}$, the MLVs spontaneously spread on the surface and become flat giant unilamellar compartments (FGUVs, Figure 1c). In either case (Figure 1b or 1c), the interaction of the membrane with the surface is enhanced with Ca^{2+} ions which connect the lipid head groups to the solid substrate, and thereby establish
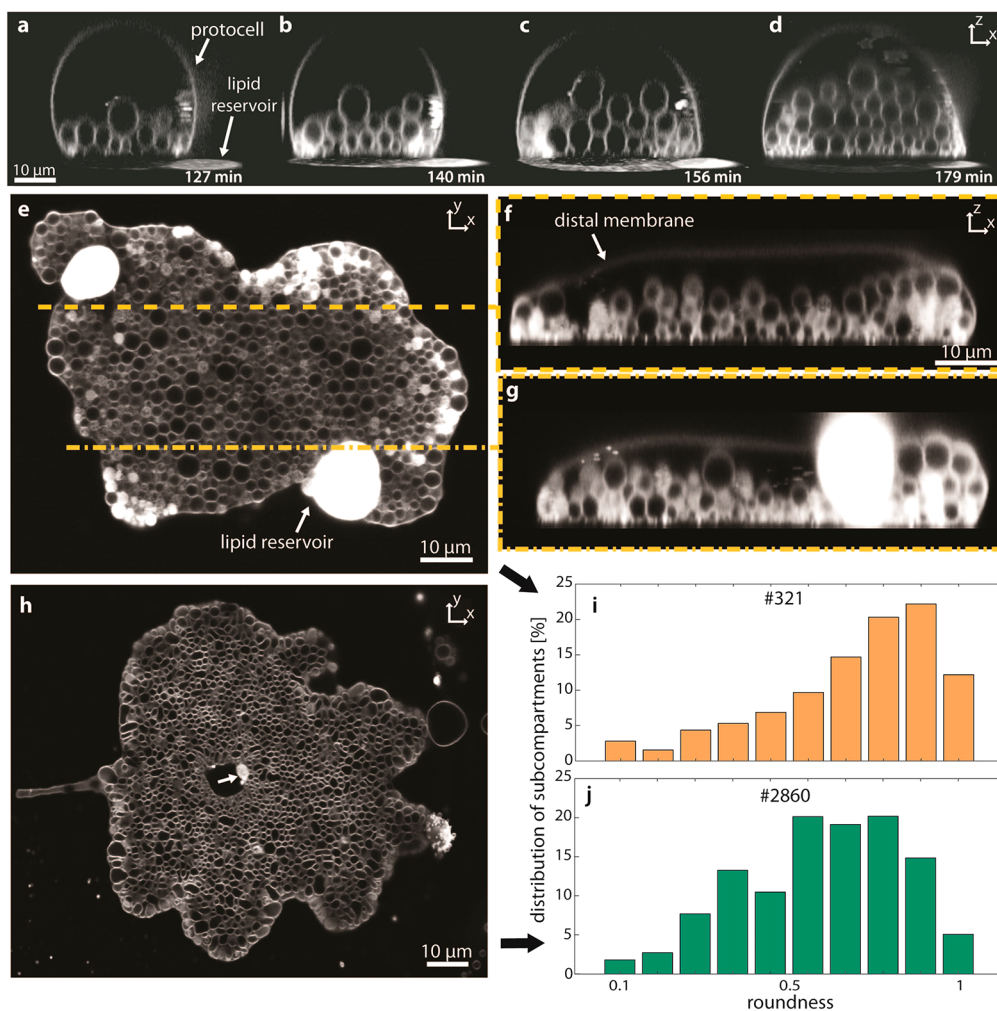
Figure 2. Formation of protocell superstructures. (a−d) Confocal micrographs showing the gradual formation of subcompartments over time (x−z cross sectional view). The protocell enveloping the subcompartments is connected to a multilamellar lipid reservoir. Over time, multiple layers of spherical subcompartments form inside the protocell from the bottom (solid surface) up. Eventually the compartments fill up the original protocell volume. (e, h) Confocal micrographs of large protocell superstructures (x−y cross sectional view) 24 h after the addition of Ca^{2+} chelators. (f, g) x−z cross sectional view along the dashed lines in panel e. Up to 3 layers of subcompartments were observed in this experiment. (i, j) Roundness analyses of the superstructures shown in panels e and h, respectively. The structures in panel e have subcompartments with higher roundness (closer to 1). The number of compartments in panel e is 321 and in panel h, 2860. In panel h the multilamellar reservoir is mostly consumed (white arrow).

pinning points at the solid−membrane interface, promoting the adhesion of the vesicles to the solid surface.[16−20] The addition of Ca^{2+} chelators[21] to the ambient environment initiates the formation of superstructures (Figure 1d).

As a result of the process described above, we experimentally observe the formation of up to several thousand micrometer-sized subcompartments inside a single unilamellar mother vesicle (Figure 2) (cf. S1 for all utilized lipid compositions and type of surfaces). Figure 2 shows the morphogenesis of the surface-adhered compartments after the surface adhesion was reversed: the surrounding Ca^{2+}-buffer was gently exchanged with a Ca^{2+}-free equivalent containing metal chelator molecules instead. The chelator forms a highly stable complex with Ca^{2+} and removes the pinning points from the nanogap between the membrane and the solid surface. This causes gradual dewetting of the surface, and spontaneous formation of subcompartments.[18,22] Figure 2a−d shows confocal micrographs of the subcompartmentalization over time, corresponding to Figure 1d. We recently reported on a related

phenomenon, where unilamellar vesicles with no access to excess lipid material constituted model compartments, leading to the formation of subcompartments spread out on the basal membrane of the parent vesicle.[22] In the current study, each mother protocell is physically connected to a multilamellar lipid reservoir. The reservoirs act as a material source, thus enabling the formation of densely packed layers of vesicular subcompartments inside the original compartment (Figures 1d and 2), and alleviate membrane tension upon external stress factors. Over the course of a few hours, almost the entire volume of the initial model protocell is filled from the surface up (Figures 1d and 2a−d).

In the case that the mother protocell spreads on the solid substrate before the chelators act ($\sigma_{adhesion} > \sigma_{reservoir}$), drawing lipid material from the multilamellar reservoir, the protocell membrane can expand across the xy plane over a wide area of several hundreds to thousands of square micrometers in the form of a flat unilamellar vesicle.[23] This initial spreading is followed by the subsequent steps of chelation, dewetting, and
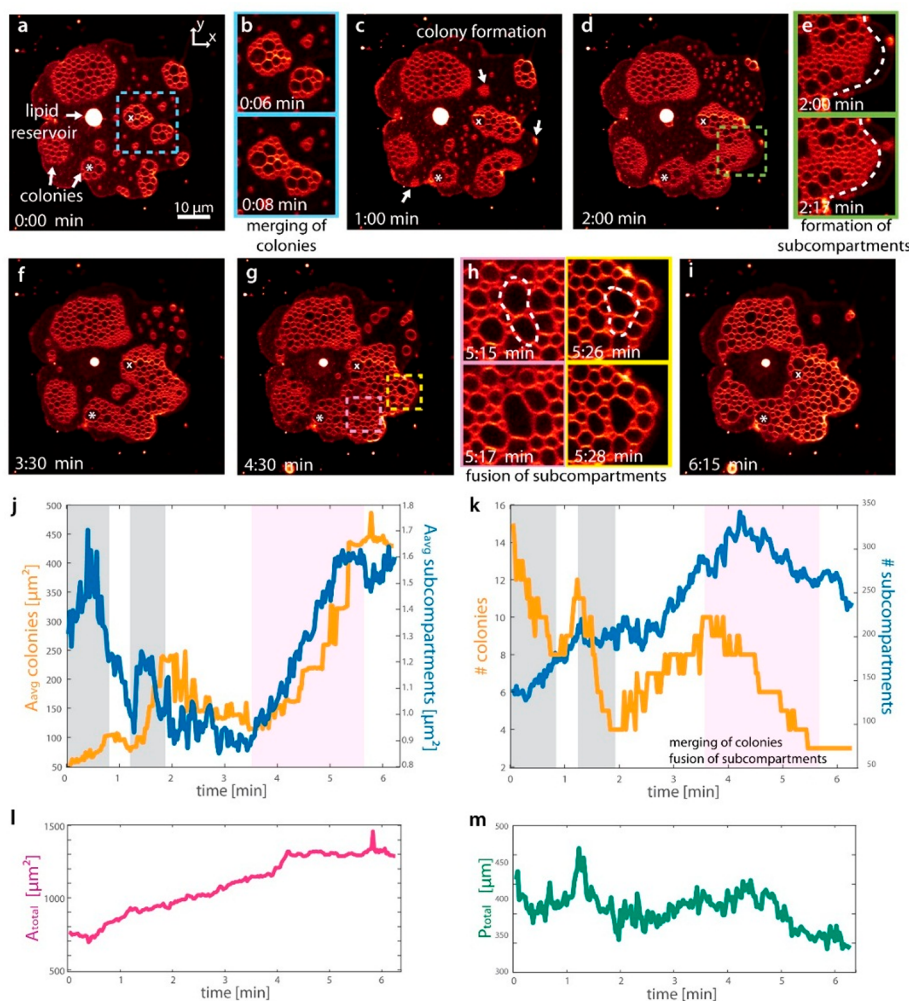
Figure 3. Growth and dynamics of protocell superstructures. (a−i) Confocal microscopy time series showing the emergence, growth, and fusion of protocell superstructures ($x−y$ cross-sectional view). The regions framed in dashed lines in panels a, d, and g are shown in panels b, e, and h, respectively. (b) Merging of two initially isolated colonies. (e) Emergence of new compartments leading to the expansion of a colony. (h) Fusion of two adjacent subcompartments. Two selected subcompartments, marked with × and ∗, have been monitored throughout the experiment in panels a−i. (j) Average area of colonies (orange plot) and average area of individual subcompartments (blue plot) vs time. The gray zones ($t < 3$ min) indicate the time periods during which new subcompartments are continuously forming. The pink zone ($t > 4$ min) indicates the period in which growth and expansion of existing clusters are observed. (k) Number of colonies (orange plot) and subcompartments (blue plot) vs time. (l) Total area of the colonies vs time. (m) Total perimeter of the colonies vs time.

formation of subcompartments. Figure 2e−h contains two examples of resulting structures. Figure 2f,g shows the cross-sectional profile views along the dashed lines in Figure 2e. Multiple layers of subcompartments can be observed within the protocell internal volume, similar to the structure in Figure 2d, just extended over a wider surface area. Figure 2i,j depicts the distribution of roundness values[24,25] of the individual compartments in Figure 2e,h (cf. Section S2 for additional micrographs and analyses). The internal compartments in panel e adopt more round shapes as compared to the ones in panel h (perfectly round, 1; elongated, <1). If initial spreading is hindered, for example, due to surface impurities, roughness, or pinning,[26] the spreading slows down or stops. At that point the excess membrane material is consumed as subcompartments continue to form and fill the constrained volume inside the envelope (Figure 2h). As more compartments form, they exhibit shape deformations with reduced roundness values. We show shape analyses using the concept of roundness to quantify the differences visually apparent from the images.

Although a vesicle morphology deviating from a spherical shape is energetically unfavorable, the system continues generating vesicles in order to overcome the energy cost of highly curved nanosized membrane instabilities. This continues as long as there is sufficient membrane material, i.e., multilamellar reservoir. Therefore, in all cases where strongly deformed vesicles are present, they are in comparatively high numbers and MLVs are largely depleted (Figure 2h and Figure S2).

We term these lipid architectures, which emerge from the surface up, "protocell superstructures" (Figures 1 and 2). Superstructures contain a multitude of densely packed membranous subcompartments of similar shape and size, enveloped in an intact lipid bilayer (Figures 1d and 2a−g). The clustering internal components physically originate from the same membrane reservoir and are formed in an autonomous fashion. The subcompartments resemble colonies of single cell organisms. We therefore term these lipid vesicle clusters "colonies", which mostly remain even after the enveloping

bilayer disintegrates. We define protocell colonies as clustering lipid compartments which originate from the same membrane, as they carry most fundamental features of microbial colonies. A microbial colony descends from a single cell,[27] and is physically densely packed together on a surface. Since the oldest fossils are of microbial nature, in the context of the origin of life, the observation of microbial colony-like protocell structures is meaningful and was previously hypothesized[4,5] but was not experimentally observed. Damer and Deamer hypothesize that protocell colonies—which they term "protocell aggregates"—could have possibly acted as a transition structure in biogenesis.[5] The authors discuss that the process of biogenesis could have begun with simple protocell aggregates developing toward robust microbial mats that leave the fossil imprints of stromatolites, represented in the rock record. They argue that the protocell aggregates enable protocell-to-protocell interaction through a form of network selection and niche construction.

The subcompartments are held together by the enveloping membrane of the original model protocell, which creates a physical superboundary. This outer membrane shell can, however, disintegrate to free the subcompartments as independent daughter cells,[22] which maintain their connection to the solid surface while remaining in close proximity to each other (cf. Figure S3).

Growth and Dynamics of Superstructures. Growth and merging of small subcompartment colonies inside the flat giant unilamellar model protocell compartments were followed by confocal microscopy (Figure 3, Movie S1). Figure 3a–i depicts an example in which more than 300 subcompartments form over the course of a few minutes (top view). Magnifications in Figure 3b,e,h show the regions framed in dashed lines in Figure 3a,d,g. Panel b shows merging of small colonies (>3 subcompartments), panel e the expansion of existing colonies due to the formation of new subcompartments, and panel h fusing subcompartments within the colonies. A mild temperature increase was applied during the experiment shown in Figure 3 in order to shorten the transformation time period of the experiment.[22,28] Figure 3j shows the average (arithmetic mean) area of the isolated colonies (orange plot) as well as the average area of each subcompartment (blue plot) in Figure 3a–i over time. The graph in Figure 3k shows the number of colonies (orange plot) and the number of individual subcompartments (blue plot). The gray zones in both graphs indicate the time period during which colonies merged and grew in size. Upon merging, the total number of colonies is reduced. The zone depicted in pink covers the period in which the subcompartments were fusing (growth in average size, drop in number), and the colonies were merging (number of colonies decreasing, and their size increasing). The total area occupied by the colonies was increasing over time (Figure 3l). After the consumption of most of the lipid reservoir (arrow in Figure 3a), it remained constant (>~4 min). The total perimeter of the colonies decreased over time (Figure 3m). Figure 3l,m shows that the superstructure minimizes its surface free energy over time by minimizing its surface area to perimeter ratio. Any lipid assembly will tend to adapt to a conformation where the surface area-to-volume ratio is minimal. For the surface adhering flat vesicles shown in Figure 3, the total membrane area grows due to formation of new compartments. In order to keep the membrane surface area minimal, continuous membrane remodeling by the assemblies is observed: merging of different colonies (Figure 3b),

rounding of the circumference (Figure 3e), and fusion of adjacent compartments (Figure 3h) which generally leads to minimization of the overall perimeter. Movie S1 and Section S4 contain five additional examples of formation and merging of the colonies. The dynamic motion of clusters, i.e., merging and collective motility, resembles the behavior reported for bacteria populations.[29,30] Another example, which we deem morphologically and dynamically similar, is surfactant foam.[31,32]

Continuum Theory for the Onset of Subcompartment Formation. To explain the dynamics of the early subcompartment formation, we developed a continuum theory that couples the elasticity of membrane deformations with the induced viscous flow of the solvent underneath the membrane. When the proximal (surface-adhered) lipid bilayer is detached from the substrate due to removal of pinning points, the thermal energy $K_B T$ (K_B, Boltzmann's constant; T, temperature) must result in fluctuations in the lipid bilayer membrane, causing it to lift off at a height h from the underlying charged substrate (Figure 4). We considered that an elastohydrodynamic instability can amplify these fluctuations and lead to the onset of inward growth of subcompartments. The three potential causes for the instability can be (i) electrostatic repulsion between the membrane and the substrate, (ii) a possible spontaneous curvature c_0 of the membrane,[33] and (iii) attractive vdW interactions between the membrane and the substrate when the distance in-between is about the bilayer thickness ($h \lesssim 10$ nm). The role of electrostatic repulsion can be omitted due to screening by the ionic ambient solution, since the bilayer thickness is much bigger than the Debye screening length of the solvent $\lambda_D = 0.84$ nm.[34] Furthermore, the lipid composition in each monolayer leaflet of the membrane is identical; therefore, the spontaneous curvature c_0 must be zero. Even if c_0 were finite on a flat membrane, the energy gain, e.g., at a crest of a plane wave undulation with a curvature c_0, would be balanced by the energy cost at a neighboring trough with the curvature c_0. Consequently, the wavelike undulation would altogether be suppressed by the membrane bending energy. On the other hand, in our system, the vdW interactions between the lipid bilayer and the aluminum substrate are attractive (set by the Hamaker constant $A_H \approx 3.8 \times 10^{-21}$ J > 0) and thus destabilize a free interface that confines a liquid:[35,36] Since vdW interactions decay with increasing distance, any forming crest would be attracted to the substrate less than the neighboring troughs, creating a pressure gradient from the crests to troughs. This in turn leads to an influx of the aqueous ionic background solvent under the proximal membrane (characterized by the vesicle radius $L \gtrsim 1$ μm, Figure 4a), reinforcing the membrane fluctuations in a positive feedback cycle. The bilayer–solvent interfacial tension is $\gamma \approx 0$; thus, a perturbed membrane region could bulge indefinitely as soon as it acquires a spherical profile during growth, since the Laplace pressure across the membrane bilayer would then vanish when $c_0 = 0$.

To quantify the size of bulging at the proximal membrane of a lipid bilayer vesicle, we developed an elastohydrodynamic thin film theory that relates the membrane bending and the attractive vdW interactions to the pressure gradients driving solvent flow in a high-aspect-ratio domain ($h \ll L$) (Figure 4a). For simplicity, we took a two-dimensional (2D) cross-section of the proximal membrane and assumed that chelation occurs uniformly along the horizontal direction at time $t = 0$ of the simulations. The small fluctuations are represented by a
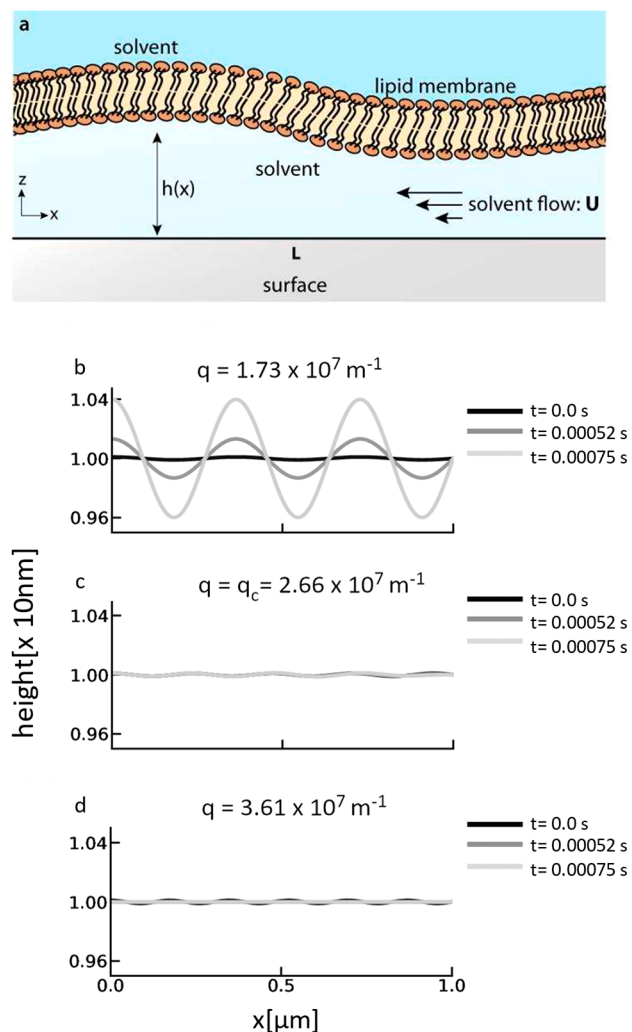
Figure 4. Elastohydrodynamic instabilities as a mechanism for subcompartment formation. (a) Bilayer−solvent (water)−substrate system. At the proximal membrane, the lipid bilayer and the solid surface confine a thin film of aqueous ionic solvent, which flows in response to the pressure gradients along the x-direction. The center point at the base of the vesicle corresponds to the left boundary, and the right boundary is located in proximity to the vesicle front. (b−d) Numerical results for the height of the membrane in linear deformation regime. Height profiles for (b) $q < q_c$, (c) $q = q_c$, and (d) $q > q_c$ at three different times. The center point at the base of the vesicle corresponds to $x = 0$ μm, and the vesicle front is located at $x = 1$ μm. The grayscale corresponds to three different times $t = 0$ s, $t = 0.00052$ s, and $t = 0.00075$ s, respectively. The results from numerical solutions show emergence of the instability below the critical wavenumber $q_c = 2.66 \times 10^7$ m^{-1}, equivalently above critical wavelength $\lambda_c = 2\pi/q_c \approx 236$ nm.

dynamic term $h_1(x, t) \ll h$ that serves as a correction term to the equilibrium bilayer height $h_0 > 0$, that is, $h = h_0 + h_1$. In the limit $\parallel \ll h_0 \ll L$, the mass conservation of the incompressible solvent−bilayer system and the flow induced by the pressure gradients due to membrane bending and vdW interactions yield the linear evolution equation:

$$\frac{\partial h_1}{\partial t} - \frac{kh_0^3}{3\mu}\frac{\partial^6 h_1}{\partial x^6} + \frac{A_H}{6\pi\mu h_0}\frac{\partial^2 h_1}{\partial x^2} = 0 \qquad (1)$$

for the height fluctuation profile h_1, where $k \sim 1.2 \times 10^{-19}$ J is the membrane bending modulus, and $\mu \sim 10^{-3}$ Pa s is the dynamic viscosity of the aqueous solvent. The onset of bulging can be determined by the linear stability analysis of eq 1 when the height undulations h_1 represent plane wave deformations, such that $h_1 = |h_1|e^{(iqx+st)}$, q being the wavenumber and s being the inverse time scale of fluctuations. Substituting h_1 in eq 1 returns the dispersion relation with a critical wavenumber q_c

$$s = \frac{kh_0^3}{3\mu}q^2(q_c^4 - q^4), \qquad q_c = \frac{1}{h_0}\left(\frac{A_H}{2\pi k}\right)^{1/4}. \qquad (2)$$

Equation 2 reveals that when $q < q_c$, $s > 0$; i.e., the vdW interactions dominate the membrane bending, destabilizing the interface. Conversely, when $q \geq q_c$, $s \leq 0$, and the bending energy would suppress the membrane fluctuations against the attractive vdW interactions. Using the experimental values $h_0 \approx 10$ nm, $A_H \approx 3.8 \times 10^{-21}$ J, and $k \approx 1.2 \times 10^{-19}$ J[37] returns $q_c = 2.66 \times 10^7$ m^{-1}, and equivalently $\lambda_c = 2\pi/q_c \approx 236$ nm. This means that the size of the perturbed membrane regions larger than ∼236 nm will lead to the growth of subcompartments. We cannot determine the exact size of the nucleating compartments with confocal microscopy, as compartments smaller than the resolution limit (150 nm) will not be distinctly visible; however, we can confirm that the smallest subcompartments we can observe are of submicron size (Figure 3d).

To investigate the dynamics of the bilayer height profile h in the presence of attractive vdW interactions, we solved eq 1 numerically in the stable regime $q \geq q_c$ and in the unstable regime $q < q_c$. The simulation details, the initial condition for h_1 determined by the thermal fluctuation spectra, and the physical boundary conditions for eq 1 are summarized in the Materials and Methods section. Figure 4 presents the time evolution of the membrane height h for the wave numbers $q = 1.73 \times 10^7$ m^{-1} (Figure 4b), $q = q_c = 2.66 \times 10^7$ m^{-1} (Figure 4c), and $q = 3.61 \times 10^7$ m^{-1} (Figure 4d). Below the critical wavenumber $q < q_c$, the inverse time scale s is positive such that fluctuations grow in time, leading to an instability (Figure 4b). In this regime, the flow profile due to the pressure gradient further amplifies the height undulations (Figure S5.2g). At the critical wavenumber $q = q_c$, the height profile remains stationary since s vanishes (Figure 4c, eq 2). This steady state is characterized by zero pressure and vanishing flow throughout the system (Figure S5.2e,h). In Figure 4d, s is negative ($q > q_c$), and the fluctuations die out as the resulting flow suppresses the height undulations (Figure S5.2i). These results suggest that the height instability triggered by the attractive vdW interactions between the lipid bilayer membrane and the aluminum substrate is a plausible mechanism for the nucleation of subcompartments. We also performed stability analyses for the screened electrostatic interactions and the effect of the spontaneous curvature. We validated that both effects stabilize the bilayer profile at a linear order (see Section S5).

Mechanical Stability of the Superstructures. To characterize the durability of the protocell superstructures in alternating aqueous environments, we investigated the effect of different osmotic conditions on the protocell superstructures (Figure 5). Isolated giant unilamellar vesicles (Figure 5a,b) and enveloped and nonenveloped vesicle colonies (Figure 5c−e) were consecutively exposed to hypotonic (low salt) and hypertonic (high salt) solutions. Figure 5f shows the duration
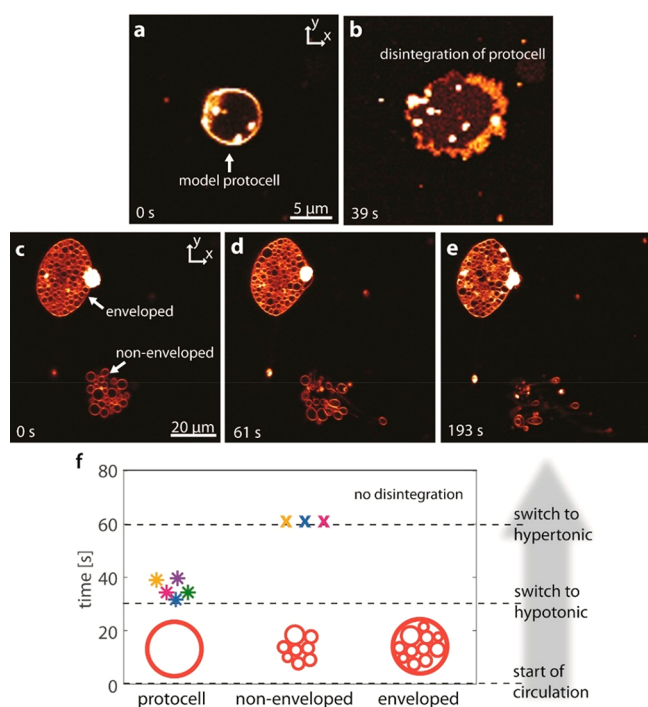
Figure 5. Mechanical stability of protocell superstructures. Confocal micrographs of (a, b) an isolated lipid compartment and (c−e) protocell superstructures (enveloped) and colonies (nonenveloped). (f) Time periods of each type of model protocell structure in panels a−e during exposure to hypo- and hypertonic environments. The gray arrow shows the order of events along the *y* axis (time). At *t* = 0 s, the structures are exposed to a gentle hydrodynamic flow via an open volume microfluidic device. At *t* = 30 s, the structures are exposed to a hypotonic solution, upon which the isolated protocells disintegrate (asterisks). At *t* = 60 s, the protocell superstructures and colonies are exposed to hypertonic solution. Shortly thereafter, the protocell colonies are disassembled (crosses). The superstructures maintain their integrity as long as 210 s at which the experiment is terminated.

for which each of the structures remains intact under the applied osmotic stress.[38−41] All structures were initially exposed to a gentle hydrodynamic flow (10−100 nL/s) from an open-volume microfluidic device for 30 s.[42] The lipid structures were then exposed to a hypotonic solution for 30 s, upon which all isolated lipid vesicles immediately ruptured (asterisks in panel f). The effect of imbalanced osmotic conditions on the deformation or rupture of individual compartments has been discussed previously.[43] Both the nonenveloped and enveloped colonies maintained their integrity during this period. Subsequently, a hypertonic solution was applied, which rapidly caused the nonenveloped vesicle clusters (Figure 5c) to decluster and some to disintegrate (Figure 5d,e). The superstructures (enveloped in a bilayer) remained intact for another 2 min (cf. Movie S2 for the entire period).

The results shown in Figure 5 support the earlier hypotheses that protocell colonies have a higher mechanical stability.[44] Even the nonenveloped structures withstand the applied ambient stress conditions better than the individual vesicles. This might be due to the presence of lipid nanotubes which tether each compartment to the surface. Membrane nanotubes can act as reservoirs to balance the membrane tension and increase robustness of lipid compartments.[45] The enveloped

superstructures exhibited higher mechanical stability compared to nonenveloped colonies upon hypertonic shock (Figure 5e). This suggests that the enveloping membrane of the superstructure protects the colony from the initial osmotic shock by acting as a barrier, and reshapes itself in response,[46] possibly also relieving membrane tension by drawing additional lipid material from the attached multilamellar reservoir. It was shown recently that hypertonic conditions cause the compression of magnetically assembled vesicle clusters and decrease the permeability into the cluster.[13] In contrast, vesicle colonies bridged by homopolyamino acids exhibited less physical stability than single compartments when exposed to osmotic stress, likely due to membrane perturbations caused by anchoring of the amino acids.[7]

Encapsulation of Compounds. Chemical information exchange within cell colonies or across generations requires distinct compartments of reactants. We studied the ability of the superstructures to encapsulate compounds from the ambient environment, e.g., DNA (Figure 6, Movie S3) and fluorescein (Figure S6). Encapsulation of genetic fragments is considered an important step in the evolution of primitive cells.[47] A membrane-bound compartment provides confinement, and protection from parasitic genetic fragments, and can increase reaction rates, which could have greatly enhanced protocell evolution, e.g., in an RNA world.[48,49] RNA encapsulation and distribution in similar lipid systems were recently reported.[28]

In order to perform the encapsulation experiments, we conceived a method to address a single superstructure with fluorescently labeled ssDNA (20 nucleobases).[50,51] We used a hydrodynamically confined flow device for local superfusion.[42,52−54] This way, we achieved complete control over the chemical environment around a selected superstructure without buildup of the superfusion agents in the ambient buffer. We can turn on/off the superfusion (gray background in Figure 6i) and observe the results in real time with confocal microscopy. The results are shown in Figure 6a−h as confocal microscopy time series (cf. Movie S3 for results of multiple experiments). The encapsulation of DNA is visible by the strong fluorescence intensity increase inside the affected subcompartments (Figure 6b,c). Encapsulation seems to be only occurring at the surface-adhered vesicle. However, we note that the image is a 3D reconstruction of thin sections which takes considerable time to assemble. During the experiment, the subcompartments inside the superstructure are not static. They are fusing (Figure 6d,e), moving, and become replaced by other compartments (Figure 6f,g). During the 3D imaging, only the vesicles at the very bottom remain in place due to surface adhesion.

The graph in Figure 6i shows the fluorescence intensity of the labeled (FAM-) DNA, according to the encapsulation experiments depicted in Figure 6a−h. The plots in the blue color range indicate the subcompartments which take up DNA during superfusion and lose it rapidly when the flow is terminated. The subcompartments represented by the plots in the red color range encapsulate the DNA and accumulate it which leads to the increase of fluorescence intensity in the internal volume with each superfusion event, represented by the gray background. The ability to maintain the internalized constituents is associated with the sealing of the initial membrane invaginations.[22]

Transient pore- and defect-mediated encapsulation of external compounds in surface-adhered protocells has been
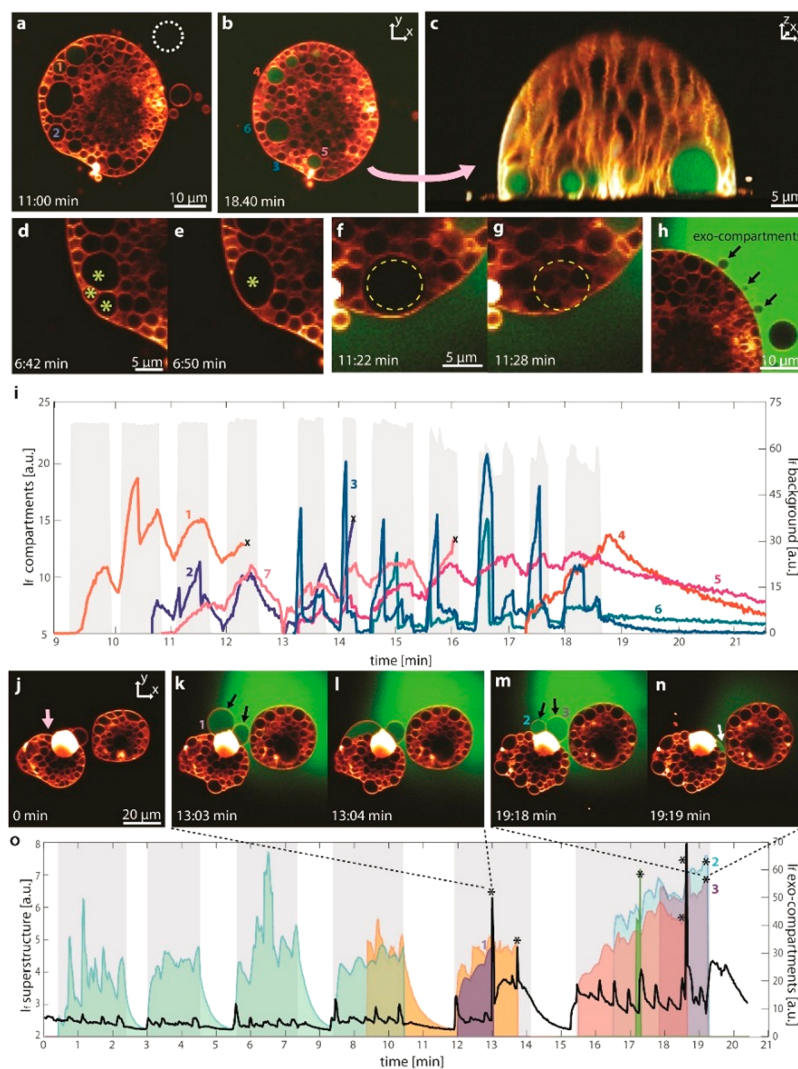
Figure 6. DNA encapsulation. (a−h) Confocal micrographs showing the fluorescently labeled DNA spontaneously encapsulated inside protocell superstructures. Micrographs show a superstructure after 11 min (a), and after 18 min (b), of DNA exposure. (c) Confocal micrograph in *y−z* cross sectional view, showing the compartments encapsulating labeled (FAM-) DNA. Close up view of (d, e) merging subcompartments, (f, g) a large subcompartment spontaneously substituted with multiple small subcompartments, and (h) exocompartments. (i) Graph showing the FAM-DNA fluorescence intensity in panels a−h during minutes 9−21 of exposure to DNA (cf. Section S7 for the graph showing the full time period and 19 compartments). The width of the gray zones indicates the duration of DNA superfusion, and their height, the intensity of the DNA in the ambient solution (*y* axis on the right of the graph: background fluorescence I_f). Each of the colored plots corresponds to a subcompartment in panels a and b. The number of each plot matches the associated compartment labeled with the same number in panels a and b (an exception is plot 7 which is not visible in panels a and b). Plots in the blue spectrum represent the subcompartments that take up the DNA and immediately lose it once superfusion is terminated. Plots in red spectrum represent subcompartments which maintain DNA even though the superfusion is terminated. The plots marked with × show subcompartments which spontaneously disappeared/relocated and could not be monitored further. (j−n) Confocal micrographs showing the fusion of exocompartments to the protocell superstructure and redistribution of contents (arrow in panels k, m, and n). (o) FAM-DNA fluorescence intensity of the superstructure marked with a pink arrow in panel j, over time. The black plot shows the average FAM-DNA intensity inside the superstructure. The gray zones indicate DNA superfusion periods (green background in panels k−n). The areas under the plots have been colored to facilitate visualization. Each colored plot shows the FAM-DNA intensity of an exocompartment vs time. The time points at which the exocompartments are merging with the protocell superstructure are marked with an asterisk.

reported both for small fluorescent dyes and genetic polymers.[22,28] This means that regardless of the position of the membrane, i.e., proximal or distal, there will be pore-mediated uptake by the enveloping membrane of the superstructure. In our previous work, we showed that subcompartments can also exchange compounds through the nanosized gap between the surface and the lipid compartment above it.[22]

Subcompartments in the early development stage maintain a large opening toward the surface. For these species, both uptake and loss of external compounds are rapid (plots in blue color range). In later stages (layers further above the surface), the large openings close due to energy minimization.[22] For these species, the uptake and loss of external compounds are comparatively slower (plots in red color range). On one hand, we observed an instant loss of internal compounds as soon as superfusion is terminated. On the other hand, we measured a
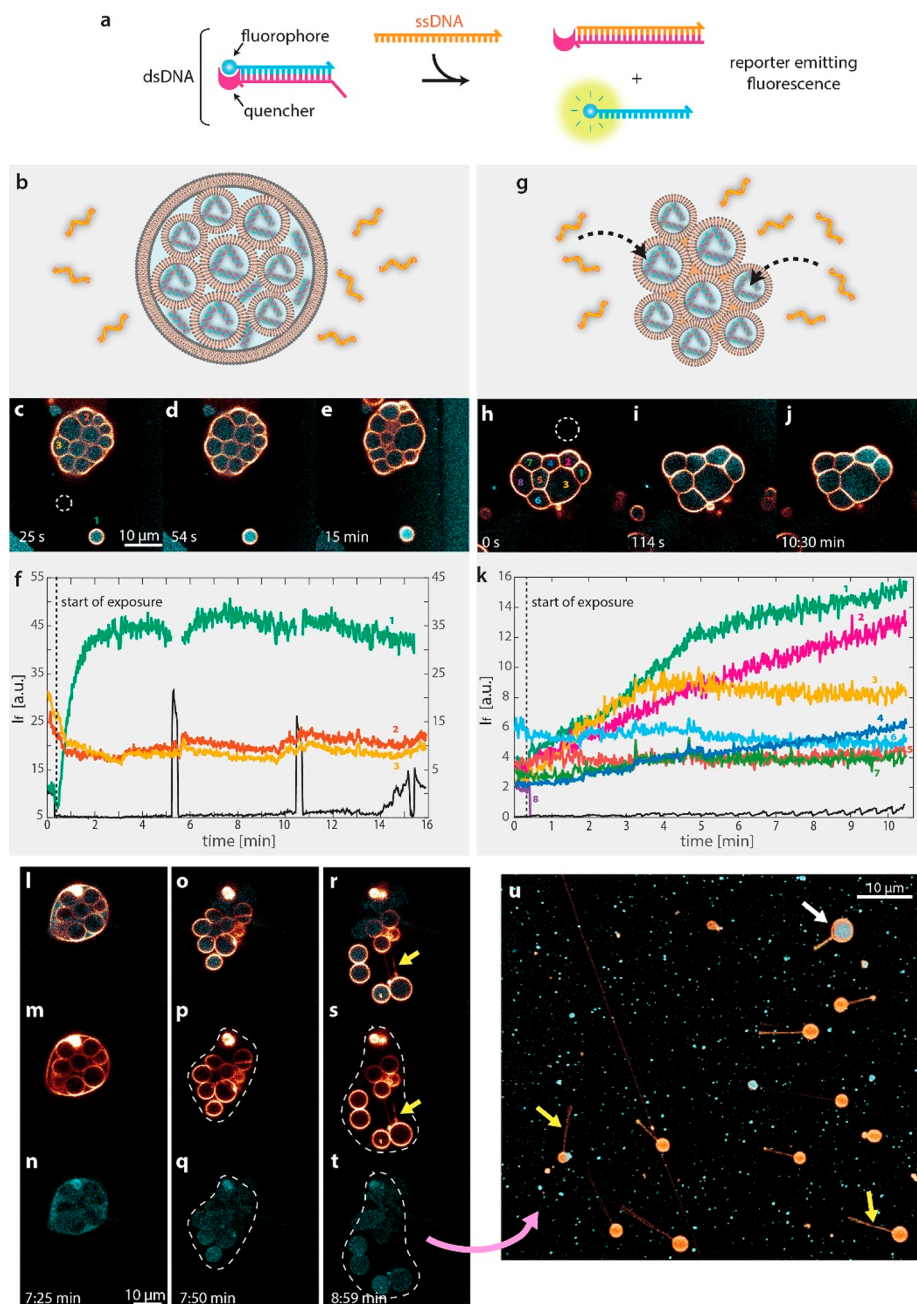
Figure 7. DNA strand displacement reactions and pseudodivision. (a, b) Schematic drawing of the displacement reaction. ssDNA reacts with (the toehold of) the dsDNA and hybridizes with the quencher DNA strand. The initially quenched fluorescent DNA strand will be released, leading to an increase in the measured fluorescence intensity. (b) A protocellular superstructure and (g) a vesicle colony encapsulating dsDNA are externally exposed to ssDNA. (c−e, h−j) Confocal micrograph time series showing two different experiments corresponding to panels b and g. In panels c−e, an isolated lipid vesicle (marked as 1) is positioned next to the superstructure. (f, k) Fluorescence intensity vs time, corresponding to panels c−e and h−j. For each experiment, the fluorescence intensity of the ambient solution (black plots in panels i and j) was measured at the region in panels c and h encircled in dashed white lines. The numbers in the micrographs denominate regions of interest; the corresponding plots have matching numbers. (l−u) Pseudodivision of a superstructure containing the reporter DNA. (l, o, r) DNA and membrane fluorescence channels as overlay. (m, p, s) Membrane fluorescence channel. (n, q, t) DNA fluorescence channel. (u) Daughter cells migrated and anchored to the surface. Yellow arrows point to the nanotubes connected to each daughter cell. The white arrow points to the daughter cell which has maintained its DNA cargo.

gradual decrease in fluorescent intensity. All uptake mechanisms are likely involved in the DNA encapsulation shown in Figure 6.

We also observed the unusual formation of "exocompartments" which extended out but remained connected to the outer membrane of the superstructure (Figure 6h,j−n). These exocompartments readily internalize ambient DNA, merge with the protocell superstructure, and in this process transfer the internalized cargo into the superstructure (Figure 6l,n) (cf. Movie S3). These uptake and delivery events can be followed from the graph presented in Figure 6o. As in Figure 6i, the superfusion events are marked with a gray background, where each colored plot represents an exocompartment. The exocompartments, reminiscent of cell membrane blebs,[55]

show that protocell superstructures can continuously generate external compartments which can uptake ambient compounds and deliver the compounds to the superstructures by merging with them. They appear to function as capture/gateway containers. It is very striking that such containers spontaneously form in an ordinary superfusion environment. Formation of exocompartments can be an osmotically driven phenomenon where slightly different concentration of solutes in the buffer, e.g., 10 mM EDTA 7 mM BAPTA inside the colonies versus 0 mM EDTA/BAPTA in the DNA buffer, causes swelling of the vesicles.[56] There is also a remote resemblance to extracellular vesicles which are ubiquitous throughout all three domains of life.[57,58] In eukaryotic cells, extracellular compartments are employed for cellular communication, e.g., during cell differentiation, mostly by formation of microvesicles with a size bracket up to 1 μm.[59] Formation of larger compartments from the plasma membrane, comparable in size with giant vesicles, has been reported in breast cancer cells.[60]

DNA Strand Displacement Reactions. The multi-compartmentalized protocell superstructures can encapsulate both single- and double-stranded DNA, and are able to accommodate strand displacement reactions[61] (Figure 7). We have selected this nonenzymatic process as an example for reactions involving prebiotically relevant molecules. It requires few reactants, and monitoring its outcome by confocal microscopy is straightforward. Initially, the superstructures were grown in an aqueous environment containing dsDNA (Figure 7a). The dsDNA consists of a fluorescently labeled strand which is initially quenched by its complementary strand, "the quencher" featuring an overhanging region, i.e., a toehold (Figure 7a). Subsequently, an invading strand, which is complementary to the quencher strand of the dsDNA, was locally superfused with the protocell superstructures and colonies. The invading strand hybridizes with the quencher strand, causing melting of the initial dsDNA, followed by release of the fluorescently labeled strand and fluorescence emission (Figure 7a). First a superstructure encapsulating dsDNA consisting of internalized vesicles in an envelope membrane is locally superfused with the strand replacement reaction catalyst (Figure 7b−f). In close proximity, it is a single GUV (Figure 7c−e) which serves as a local control. While the control vesicle shows immediate strong fluorescence increase (plot 1 in green in Figure 7f), the enveloped structure maintains its low fluorescence. In the second experiment, which was conducted with the same superfusion protocol, the colony is lacking the envelope (Figure 7g−k). We see a fluorescence signal increase over time in 2 of the 7 single-shell compartments in the superstructure (plots 1 and 2 in Figure 7k). The unenveloped vesicles contain a single bilayer shell, similar to the single control vesicle in Figure 7c−e. The ssDNA in this case crosses a single membrane barrier versus a double membrane in the enveloped structures. In summary, ssDNA can be encapsulated within the protocell colonies lacking an enveloping membrane, but cannot be easily encapsulated within the ones which are enveloped by an additional lipid bilayer. According to the results, there appears to be a distinction between the protocell colonies and the superstructures in terms of ssDNA encapsulation and hosting reactions catalyzed by such DNA strands. On one hand, the inability to encapsulate a genetic polymer and host non-enzymatic genetic reactions can be a disadvantage for protocell superstructures in comparison to the isolated protocells or protocell colonies. On the other hand, this provides protection against parasitic genetic polymers, hence enabling differential survival. Thus, given that natural selection is one of the key mechanisms of evolution, a simple means of it in the context of the origins of life emerges based on this observation.

Pseudodivision of Superstructures. Figure 7l−u shows one superstructure undergoing pseudodivision[22] (Figure S3). This occurs when the enveloping membrane ruptures and the subcompartments migrate and eventually become free, surface-anchored daughter cells. Figure 7l−t show the protocell structure 7 min 25 s after the DNA strand displacement experiment was initiated. Figure 7l,o,r shows the lipid membrane and DNA fluorescence channels overlaid; Figure 7m,p,s contains graphs of the membrane fluorescence only, and the graphs in Figure 7n,q,t represent the DNA fluorescence only. A video of the original protocell bursting and releasing the daughter cells is provided as Supporting Information (Movie S4). The daughter cells migrate and attach to other locations on the substrate. In Figure 7u, daughter cells anchored to the substrate with nanotethers are displayed. It is well established that the vesicles exposed to a hydrodynamic force move and grow nanotethers.[62] Accordingly, the nanotubes we observe are most likely formed spontaneously during migration of daughter cells. Another possibility is that they maintain the nanotethers from the original intraprotocellular formation event (arrows in Figure 7r,s). One daughter cell still carries its fluorescence content acquired prior to the pseudodivision event (white arrow in Figure 7u). Similar structures have been reported in migrating eukaryotic cells, which leave long tubular strands terminated with large cargo vesicles (migrasomes).[63] These connecting tubes eventually break, and migrasomes can transport the cytosolic content to other cells. The fluorescence concentrated in the superstructure in Figure 7n shows that the DNA is concentrated inside the superstructure and there are no residues of DNA in the external region. When the compartment ruptures, the DNA that is inside the primary volume of the superstructure—the space between the external membrane and the subcompartments—is released to the ambient environment and appears to nonspecifically adsorb to the solid surface. DNA is known to adsorb extensively on positively charged alumina[64] and aggregate on other types of surfaces.[65,66]

Giant vesicle compartments can act as miniature reactors and host various (bio)chemical systems, including intravesicular DNA strand melting and annealing,[67] reverse transcription PCR,[68] and light-triggered enzymatic reactions.[69] Figure 7 illustrates how the superstructures can consecutively encapsulate macromolecular DNA strands from the ambient environment and host a DNA displacement reaction.[70] This reaction was chosen as a relatively simple example of an enzyme-free prebiotic reaction similar to nonenzymatic RNA replication-related reactions.[71]

CONCLUSION

A tendency of biological cells toward aggregation is observed across all domains of life from bacterial colonies to multicellular organisms. The colony structure provides advantages, including greater physical stability and enhanced communication. Protocell colonies have been hypothesized as a possible development step toward the first cells.[4,5,11]

We show a consistent pathway leading to colony-like protocell superstructures under simple conditions relevant to the early Earth.

Our experimental system consists of a minimal number of prebiotically relevant components: amphiphiles, a solid surface, and an aqueous environment suitable for surfactant self-assembly. Our findings presume that phospholipids, variants of which we have used for the experiments, could have been present under prebiotic conditions.[72−75] Adhesion-promoting Ca^{2+} ions were present in early Earth minerals, which could have acted as a source in a natural prebiotic environment.[76,77] The chelator molecules used in our experiments to induce depinning were highly likely not present on the early Earth. However, clay minerals which are known to adsorb mono- or divalent cations[78] could have potentially acted as sources for chelating agents. We consider experimental studies to this respect a valuable next step to test this hypothesis.

In challenging ambient conditions, e.g., osmotic and shear stress, the protocell superstructures provide a stability, i.e., survival advantage. Differential survival is a component of natural selection, provided it affects a sequence of generations. Despite the autonomous transformations observed in this work, we cannot show at this point the continuous reproduction of protocell superstructures. It is therefore too early to speculate whether the described phenomena could be realistically linked to selection processes toward early biological cells. Nevertheless, our findings indicate a potential step in this direction.

Subcompartments grow from the bottom-up inside a model protocell and exhibit high mechanical and osmotic stability. The protocell colony structures we produced in the laboratory can encapsulate genetic polymers from the ambient environment and host nonenzymatic reactions. Upon disintegration of the enveloping membrane, subcompartments detach and migrate, carrying the encapsulated cargo to remote locations. Membranous protocell superstructures which can uptake chemical compounds and maintain them in secluded spaces may enable the development of prebiotic containers with an increasing set of functions and features toward primitive forms of life.

MATERIALS AND METHODS

Preparation of Lipid Vesicles. The dehydration and rehydration method[79,80] was used to prepare the lipid suspensions. Briefly, lipids (99 wt %) and lipid-conjugated fluorophores (1 wt %) were dissolved in chloroform to a final concentration of 10 mg/mL (cf. Table S1 for a detailed list of lipid types and membrane compositions). 300 μL of this mixture was then transferred to a 10 mL round-bottom flask, and the solvent was removed in a rotary evaporator at reduced pressure (20 kPa) for 6 h to form a dry lipid film. The film was rehydrated with 3 mL of PBS buffer (5 mM Trizma Base, 30 mM K_3PO_4, 3 mM $MgSO_4 \cdot 7H_2O$, 0.5 mM Na_2EDTA, pH 7.4 adjusted with 1 M H_3PO_4) and stored at +4 °C overnight to allow the lipid cake to swell. The sample was then sonicated for 25 s at room temperature, leading to the formation of multi- and unilamellar giant vesicular compartments. For sample preparation, 4 μL of the lipid suspension was desiccated for 20 min, and the dry residue was subsequently rehydrated with 0.5 mL of HEPES-Na buffer containing 10 mM HEPES buffer and 100 mM NaCl, adjusted to pH 7.8 with 5 M NaOH. The lipid suspension after rehydration typically contains a few unilamellar vesicles in addition to MLVs and the hybrid vesicles each comprising a unilamellar vesicle attached to an MLV. The lipid suspension was thereafter transferred onto a solid surface submerged in HEPES-Na buffer with addition of 4 mM $CaCl_2$ (pH 7.8 adjusted with 5 M NaOH). The lipid vesicles in the suspension spontaneously attach to the solid surface.

Surface Preparation. Aluminum (Figures 2,3, and 5−7) surfaces were fabricated at the Microtechnology and Nanoscience facility at

Chalmers University (MC2), Sweden, or at the Norwegian Micro- and Nano-Fabrication Facility at the University of Oslo (MiNaLab). Al_2O_3 (Figure S1) was deposited in MiNaLab. All thin films were deposited on glass coverslips (Menzel Gläser #1, WillCo Wells B.V., Amsterdam, the Netherlands). Al films prepared at MC2 were deposited by sputter deposition using an FHR MS150 instrument (FHR Anlagenbau GmbH) to final thickness 10 nm. The substrates were precleaned using an ultrasonic bath of acetone for 10 min, followed by an IPA and DI water bath, and blown dry with N_2. Subsequently they were exposed to oxygen plasma cleaning (50 W, 250 mT, 2 min). At MiNa Laboratories, Al was deposited onto the glass substrates by e-beam evaporation using an EvoVac instrument (Ångstrom Engineering), also to a final thickness of 10 nm. Prior to the deposition the glass slides were cleaned using IPA and deionized water and blown dry with N_2. Al_2O_3 was deposited onto glass substrates by atomic layer deposition (Beneq), to a final thickness of 10 nm. Surfaces were used immediately after their fabrication.

Addition of Chelators. To initiate the membrane instabilities leading to subcompartment formation, the buffer in the sample was gently exchanged with chelation buffer containing 10 mM HEPES, 100 mM NaCl, 10 mM EDTA, and 7 mM BAPTA (pH 7.8, adjusted with 5 mM NaOH), using an automatic pipete 20 min after the initial deposition of the vesicles onto the substrates.

Local Heating. For the temperature control experiments shown in Figure 3, an optical fiber coupled to IR-B laser was assembled to locally increase the temperature in the sample, in order to facilitate the dewetting and subcompartment formation. A semiconductor diode laser (HHF-1470-6-95, λ = 1470 nm, Seminex), driven with an 8 A power source (4308 Laser Source, Arroyo Instruments), was used in combination with a 0.22 NA multimode optical fiber with 50 μm core diameter (Ocean Optics). The fiber exit was positioned approximately 30−50 μm from the vesicle by means of a micromanipulator. The laser current utilized for experiments was in the range 0.7−0−9 A, resulting in a local temperature increase to 40 and 70 °C.[28,81] To avoid a heat shock, we initially set the temperature to 40 °C and a few seconds after increased it to 70 °C.

Microfluidic Device. The superfusion experiments shown in Figures 5−7 were performed using an open space microfluidic pipette (Biopen System, Fluicell AB),[42] positioned using a 3-axis water hydraulic micromanipulator (Narishige) in the vicinity of the protocell structures (30−50 μm distance). The structures were exposed to various solutes in pulses or in continuous flow, as specified for individual experiments. In the experiment illustrated in Figure S6, 25 μM fluorescein sodium salt in HEPES-Na buffer was used.

Mechanical Stability Determination. In Figure 5, the model protocells and protocell superstructures were exposed to solutions of different osmotic strength (deionized water, HEPES-Na buffer) in intervals of 30 s using the microfluidic device described above.

Genetic Polymers and DNA Displacement Reaction. The experiments involving DNA delivery shown in Figure 6 were performed using the microfluidic pipette described. The protocell superstructures were superfused with HEPES-Na buffer containing 25 μM FAM-conjugated 20 base long DNA oligonucleotide (5′-/56-FAM/TGT ACG TCA CAA CTA CCC CC-3′) (Dharmacon) (pH 7.8, adjusted with 5 mM NaOH).

In the experiments shown in Figure 7, three DNA oligonucleotides, purified with HPLC (Integrated DNA technologies), were used for the DNA displacement reaction reported by Zhang et al.[61] The reactant sequences are as follows:

- reporter-ROX: /56-ROXN/CT TTC CTA CAC CTA CG
- reporter-RQ: TGG AGA CGT AGG TGT AGG AAA G/ 3IAbRQSp/
- output: CTT TCC TAC ACCTAC GTC TCC AAC TAA CTT ACG G

A thermal cycle was run to anneal 20 μM reporter-ROX and 20 μM reporter-RQ in TE buffer containing 10 mM Tris-HCl and 1 mM EDTA (pH 8.0, adjusted with 5 mM NaOH and 1 mM HCl). The sample was incubated at 95 °C for 5 min and subsequently cooled to 20 °C over 75 min. The samples were further cooled and stored at +4

°C until the encapsulation experiment. To encapsulate DNA dimers (ROX-RQ) in the protocells and superstructures, DNA dimers were added to the chelation buffer to a final concentration of 5 μM during buffer exchange. After formation of structures, the excess dimers were removed by a second buffer exchange step, using dimer-free chelation buffer administered by an automatic pipette. 10 μM output strand (ssDNA depicted in orange color in Figure 7a,b,g) in HEPES-Na buffer was locally delivered to the vicinity of structures in pulses, using the microfluidic pipette. The product of the DNA displacement reaction was observed as fluorescence signal produced by the released reporter-ROX strand.

Microscopy Imaging. All microscopy images were acquired with a laser scanning confocal microscopy system (Leica SP8) using an HCX PL APO CS 40× oil, NA 1.3 objective. The excitation/emission wavelengths varied with the employed fluorophores: rhodamine B ex 560 nm/em 583 nm (Figures 2, 3, 5, and 6); ATTO 488 ex 488 nm/em 505 nm (Figure 7); Texas Red DHPE ex 595 nm/em 615 nm (Figure S1); FAM-DNA ex 488 nm/em 515 nm (Figure 6); and ssDNA ex 588 nm/em 608 nm (Figure 7).

Image Analyses. 3D fluorescence micrographs were reconstructed using Leica Application Suite X software (Leica Microsystems). Image enhancement of fluorescence micrographs for the figures was performed with Adobe Photoshop CS4 (Adobe Systems). The image analysis shown in Figure 2i,j and fluorescence intensity analyses shown in Figure 6i,o and Figure 7f,k were performed with NIH Image-J software. The segmentation and counting of the subcompartments and colonies for the extended growth analyses (Section S4) were performed using the DenoiSeg plugin of ImageJ.[82] The graphs were plotted using the open-source python library Matplotlib 3.5.2.

Roundness Analyses. Roundness, as determined for the subcompartments shown in Figure 2i,j and Figure S2, is defined as $4 \times area/(\pi \times major\_axis^2)$. The roundness data for each histogram were normalized to the total number of subcompartments in each graph, and expressed as percentage. The subcompartments were detected with *Classic Watershed* segmentation using the Fiji image processing package (ImageJ 1.53q). Images were first divided into smaller pieces, and their dynamic range was optimized with the single frame HDR method. Then a Gaussian blur filter (sigma: 1−3) was applied to the images to avoid oversegmentation. Thereafter, we used diagonal connectivity and modified the lowest and the highest grayscale values to improve, when possible, the quality of the segmentation in the *Classic Watershed* segmentation procedure (MorpholibJ plugin). Thresholding was applied to convert the images into 8-bit masks. Finally, the *Analyze Particles* function was used on this mask to calculate the roundness of the detected lipid compartments. The 8-bit masks were overlaid with the original pictures (using GNU Octave 7.1.0) and visually inspected to ensure correct overlap between the actual and detected vesicles. All graphs were plotted in Matlab R2018a. Schematic drawings were created with Adobe Illustrator CS4 (Adobe Systems).

Elastohydrodynamic Theory for the Membrane Dynamics. We assume that, at early time stages when the membrane deformations are small, the membrane height is given by $h(x, t) = h_0 + h_1(x, t)$ with $h_1 \ll h_0$ where h_0 is the height of undeformed membrane. In the limit $\partial h/\partial x \ll 1$, to a linear order in h_1, the pressure difference p across the lipid membrane is given by

$$p = k\frac{\partial^4 h_1}{\partial x^4} - \frac{A_H}{2\pi h_0^4}h_1 \tag{3}$$

where $k \sim 10^{-19}$ J is the bending modulus of the membrane, and $A_H \sim 10^{-21}$ J is the Hamaker constant that characterizes the vdW interactions between membrane and the aluminum substrate. The local mass conservation of the incompressible lipid membrane and the incompressible fluid underneath require that the rate of change of height h be governed by spatial variation of the liquid flux hU in the horizontal direction, where U is horizontal flow speed. To a linear order in h_1, the mass conservation of a thin liquid film is given by

$$\frac{\partial h_1}{\partial t} + \frac{\partial}{\partial x}(h_0 U) = 0, \qquad U = -\frac{h_0^2}{3\mu}\frac{\partial p}{\partial x} \tag{4}$$

where μ is the dynamic viscosity of the solvent. Equations 4 along with 3 constitute our elastohydrodynamic theory. Since the coefficients in eq 4 are independent of x and t, we explored the solutions of the form $h_1 = |h_1|e^{(iqx+st)}$, where $|h_1|$ is the fluctuation amplitude at $t = 0$ resulting from the thermal energy, q is the wavenumber of a given mode, and s is the corresponding inverse deformation time scale. In dimensionless units, substituting this relation into eq 4, we arrive at the following dispersion relation

$$s = q^2(-\beta q^4 + 3), \qquad \beta = \frac{6k\pi h_0^4}{A_H L^4} \tag{5}$$

with critical wavenumber $q_c = \left(\frac{3}{\beta}\right)^{1/4}$. For numerical implementation we used the open source finite element analysis (FEA) library FEniCS on Python 3.6.[83] At $t = 0$, the membrane height profile is given by $h(x) = 1 + 0.001 \cos(qx)$, and the time evolution is subject to the following boundary conditions: at $x = 0$ we set $U = 0$, $\frac{\partial h}{\partial x} = 0$, and $\frac{\partial^3 h}{\partial x^3} = 0$; at $x = 1$ we set $h = 1$, $p = 0$, and $\frac{\partial^2 h}{\partial x^2} = 0$.

ASSOCIATED CONTENT

Ⓢ Supporting Information

The Supporting Information is available free of charge at https://pubs.acs.org/doi/10.1021/acsnano.2c08093.

> Movie S1: growth and dynamics of protocell superstructures (AVI)
>
> Movie S2: mechanical stability of protocell superstructures (AVI)
>
> Movie S3: DNA encapsulation (AVI)
>
> Movie S4: DNA strand displacement reaction (AVI)
>
> Lipid compositions and surfaces, extended roundness analyses, pseudodivision, extended growth analyses, continuum theory for the onset of the subcompartment formation, fluorescein encapsulation, and DNA encapsulation (PDF)

AUTHOR INFORMATION

Corresponding Authors

C. Nadir Kaplan − *Department of Physics and Center for Soft Matter and Biological Physics, Virginia Polytechnic Institute and State University, Blacksburg, Virginia 24061, United States;* ⓞ orcid.org/0000-0003-1314-1497; Email: nadirkaplan@vt.edu

Irep Gözen − *Centre for Molecular Medicine Norway, Faculty of Medicine, University of Oslo, 0318 Oslo, Norway;* ⓞ orcid.org/0000-0002-5379-3273; Email: irep@uio.no

Authors

Chinmay Katke − *Department of Physics and Center for Soft Matter and Biological Physics, Virginia Polytechnic Institute and State University, Blacksburg, Virginia 24061, United States;* ⓞ orcid.org/0000-0003-0384-691X

Esteban Pedrueza-Villalmanzo − *Department of Chemistry and Chemical Engineering, Chalmers University of Technology, Göteborg SE-412 96, Sweden; Department of Physics, University of Gothenburg, Gothenburg 405 30, Sweden*

Karolina Spustova − *Centre for Molecular Medicine Norway, Faculty of Medicine, University of Oslo, 0318 Oslo, Norway;* ⓞ orcid.org/0000-0003-4456-4724

Ruslan Ryskulov − *Department of Chemistry and Chemical Engineering, Chalmers University of Technology, Göteborg SE-412 96, Sweden*

Complete contact information is available at:
https://pubs.acs.org/10.1021/acsnano.2c08093

Author Contributions

#C.K. and E.P.-V. contributed equally to this work.

Author Contributions

C.K. developed the continuum elastohydrodynamic theory-based model and performed the extended growth analyses together with R.R. E.P.-V. performed the extended roundness analyses. E.P.-V. and R.R. fabricated and characterized the solid surfaces for the experiments. K.S. carried out the microscopy experiments, analyzed experimental data, and designed the experiments regarding mechanical stability. C.N.K. proposed and established the continuum elastohydrodynamic theory-based model. I.G. suggested the investigation of the protocell colony and superstructure phenomena, designed the experiments, performed the experiments regarding DNA encapsulation together with K.S., performed data analyses and evaluation, and supervised the project. All authors contributed to the writing of the original manuscript. C.K., E.P.-V., R.R., C.N.K., and I.G. addressed the revisions.

Notes

An earlier version of this Article[84] has been posted on a preprint server.
The authors declare no competing financial interest.

REFERENCES

(1) Gánti, T. *The Principles of Life*; Oxford University Press Inc.: New York, 2003.

(2) Lopez, A.; Fiore, M. Investigating Prebiotic Protocells for A Comprehensive Understanding of the Origins of Life: A Prebiotic Systems Chemistry Perspective. *Life (Basel)* **2019**, *9* (2), 49.

(3) Lyu, Y.; Peng, R.; Liu, H.; Kuai, H.; Mo, L.; Han, D.; Li, J.; Tan, W. Protocells Programmed Through Artificial Reaction Networks. *Chemical Science* **2020**, *11*, 631−642.

(4) Monnard, P.-A.; Walde, P. Current Ideas About Prebiological Compartmentalization. *Life (Basel)* **2015**, *5* (2), 1239−1263.

(5) Damer, B.; Deamer, D. The Hot Spring Hypothesis for an Origin of Life. *Astrobiology* **2020**, *20*, 429−452.

(6) Thompson, D. A. W. *On Growth and Form*, New Edition; Cambridge University Press: Cambridge, UK, 1945.

(7) Carrara, P.; Stano, P.; Luisi, P. L. Giant Vesicles "Colonies": A Model for Primitive Cell Communities. *ChemBioChem.* **2012**, *13*, 1497−1502.

(8) Casas-Ferrer, L.; Brisson, A.; Massiera, G.; Casanellas, L. Design of Vesicle Prototissues As a Model for Cellular Tissues. *Soft Matter* **2021**, *17*, 5061−5072.

(9) Jin, L.; Kamat, N. P.; Jena, S.; Szostak, J. W. Fatty Acid/Phospholipid Blended Membranes: A Potential Intermediate State in Protocellular Evolution. *Small* **2018**, *14*, 1704077.

(10) de Souza, T. P.; Bossa, G. V.; Stano, P.; Steiniger, F.; May, S.; Luisi, P. L.; Fahr, A. Vesicle Aggregates As a Model for Primitive Cellular Assemblies. *Phys. Chem. Chem. Phys.* **2017**, *19*, 20082−20092.

(11) Wang, X.; Tian, L.; Du, H.; Li, M.; Mu, W.; Drinkwater, B. W.; Han, X.; Mann, S. Chemical Communication in Spatially Organized Protocell Colonies and Protocell/Living Cell Micro-Arrays. *Chemical Science* **2019**, *10*, 9446−9453.

(12) Bolognesi, G.; Friddin, M. S.; Salehi-Reyhani, A.; Barlow, N. E.; Brooks, N. J.; Ces, O.; Elani, Y. Sculpting and Fusing Biomimetic Vesicle Networks Using Optical Tweezers. *Nat. Commun.* **2018**, *9*, 1882.

(13) Li, Q.; Li, S.; Zhang, X.; Xu, W.; Han, X. Programmed Magnetic Manipulation of Vesicles Into Spatially Coded Prototissue Architectures Arrays. *Nat. Commun.* **2020**, *11*, 232.

(14) Bernard, A.-L.; Guedeau-Boudeville, M.-A.; Jullien, L.; di Meglio, J.-M. Raspberry Vesicles. *Biochimica et Biophysica Acta (BBA) - Biomembranes* **2002**, *1567*, 1−5.

(15) Köksal, E. S.; Põldsalu, I.; Friis, H.; Mojzsis, S. J.; Bizzarro, M.; Gözen, I. Spontaneous Formation of Prebiotic Compartment Colonies On Hadean Earth and Pre-Noachian Mars. *ChemSystemsChem.* **2021**, *4* (3), e202100040.

(16) Akashi, K.; Miyata, H.; Itoh, H.; Kinosita, K., Jr. Formation of Giant Liposomes Promoted by Divalent Cations: Critical Role of Electrostatic Repulsion. *Biophys. J.* **1998**, *74*, 2973−2982.

(17) Melcrová, A.; Pokorna, S.; Pullanchery, S.; Kohagen, M.; Jurkiewicz, P.; Hof, M.; Jungwirth, P.; Cremer, P. S.; Cwiklik, L. The Complex Nature of Calcium Cation Interactions With Phospholipid Bilayers. *Sci. Rep.* **2016**, *6*, 38035.

(18) Bilal, T.; Gözen, I. Formation and Dynamics of Endoplasmic Reticulum-Like Lipid Nanotube Networks. *Biomaterials Science* **2017**, *5*, 1256−1264.

(19) Ainla, A.; Gözen, I.; Orwar, O.; Jesorka, A. A Microfluidic Diluter Based On Pulse Width Flow Modulation. *Anal. Chem.* **2009**, *81*, 5549−5556.

(20) Lobovkina, T.; Gözen, I.; Erkan, Y.; Olofsson, J.; Weber, S. G.; Orwar, O. Protrusive Growth and Periodic Contractile Motion in Surface-Adhered Vesicles Induced by Ca2+-Gradients. *Soft Matter* **2010**, *6*, 268−272.

(21) Wilschut, J.; Duzgunes, N.; Fraley, R.; Papahadjopoulos, D. Studies On the Mechanism of Membrane Fusion: Kinetics of Calcium Ion Induced Fusion of Phosphatidylserine Vesicles Followed by a New Assay for Mixing of Aqueous Vesicle Contents. *Biochemistry* **1980**, *19*, 6011−6021.

(22) Spustova, K.; Köksal, E. S.; Ainla, A.; Gözen, I. Subcompartmentalization and Pseudo-Division of Model Protocells. *Small* **2021**, *17*, 2005320.

(23) Gözen, I.; Dommersnes, P.; Czolkos, I.; Jesorka, A.; Lobovkina, T.; Orwar, O. Fractal Avalanche Ruptures in Biological Membranes. *Nat. Mater.* **2010**, *9*, 908−912.

(24) Kindt, J. T.; Szostak, J. W.; Wang, A. Bulk Self-Assembly of Giant, Unilamellar Vesicles. *ACS Nano* **2020**, *14*, 14627−14634.

(25) Zupanc, J.; Drašler, B.; Boljte, S.; Kralj-Iglič, V.; Iglič, A.; Erdogmus, D.; Drobne, D. Lipid Vesicle Shape Analysis From Populations Using Light Video Microscopy and Computer Vision. *PLoS One* **2014**, *9*, e113405−e113405.

(26) Rädler, J.; Strey, H.; Sackmann, E. Phenomenology and Kinetics of Lipid Bilayer Spreading on Hydrophilic Surfaces. *Langmuir* **1995**, *11*, 4539−4548.

(27) Nadell, C. D.; Drescher, K.; Foster, K. R. Spatial Structure, Cooperation and Competition In Biofilms. *Nature Reviews Microbiology* **2016**, *14*, 589−600.

(28) Köksal, E. S.; Liese, S.; Xue, L.; Ryskulov, R.; Viitala, L.; Carlson, A.; Gözen, I. Rapid Growth and Fusion of Protocells in Surface-Adhered Membrane Networks. *Small* **2020**, *16*, 2002529.

(29) Feng, J.; He, Y. Collective Motion of Bacteria and Their Dynamic Assembly Behavior. *SCIENCE CHINA Materials* **2017**, *60*, 1079.

(30) Zhang, H. P.; Be'er, A.; Florin, E. L.; Swinney, H. L. Collective Motion and Density Fluctuations in Bacterial Colonies. *Proc. Natl. Acad. Sci. U. S. A.* **2010**, *107*, 13626−13630.

(31) Langevin, D. Aqueous Foams and Foam Films Stabilised by Surfactants. Gravity-Free Studies. *Comptes Rendus Mecanique* **2017**, *345*, 47−55.

(32) Winkelmann, J.; Dunne, F. F.; Langlois, V. J.; Möbius, M. E.; Weaire, D.; Hutzler, S. 2D Foams Above the Jamming Transition: Deformation Matters. *Colloids Surf., A* **2017**, *534*, 52−57.

(33) Steinkühler, J.; Knorr, R. L.; Zhao, Z.; Bhatia, T.; Bartelt, S. M.; Wegner, S.; Dimova, R.; Lipowsky, R. Controlled Division of Cell-Sized Vesicles by Low Densities of Membrane-Bound Proteins. *Nat. Commun.* **2020**, *11*, 905.

(34) Phillips, R.; Kondev, J.; Theriot, J.; Garcia, H. G. *Physical Biology of the Cell*; Garland Science: Boca Raton, 2012.

(35) Israelachvili, J. N. Van der Waals Forces. In *Intermolecular and Surface Forces*, 3rd ed.; Israelachvili, J. N., Ed.; Academic Press: San Diego, 2011; Chapter 6, pp 107−132.

(36) Oron, A.; Davis, S. H.; Bankoff, S. G. Long-scale evolution of thin liquid films. *Rev. Mod. Phys.* **1997**, *69*, 931−980.

(37) Chaurasia, A. K.; Rukangu, A. M.; Philen, M. K.; Seidel, G. D.; Freeman, E. C. Evaluation of Bending Modulus of Lipid Bilayers Using Undulation and Orientation Analysis. *Phys. Rev. E* **2018**, *97*, No. 032421.

(38) Hallett, F. R.; Marsh, J.; Nickel, B. G.; Wood, J. M. Mechanical Properties of Vesicles. II. A Model for Osmotic Swelling and Lysis. *Biophys. J.* **1993**, *64*, 435−442.

(39) Zong, W.; Li, Q.; Zhang, X.; Han, X. Deformation of Giant Unilamellar Vesicles Under Osmotic Stress. *Colloids Surf., B* **2018**, *172*, 459−463.

(40) Sarkar, M. K.; Karal, M. A. S.; Ahmed, M.; Ahamed, M. K.; Ahammed, S.; Sharmin, S.; Ul Alam Shibly, S. Effects of Osmotic Pressure on the Irreversible Electroporation in Giant Lipid Vesicles. *PLoS One* **2021**, *16* (5), e0251690.

(41) Chabanon, M.; Ho, J. C. S.; Liedberg, B.; Parikh, A. N.; Rangamani, P. Pulsatile Lipid Vesicles Under Osmotic Stress. *Biophys. J.* **2017**, *112*, 1682−1691.

(42) Ainla, A.; Jeffries, G. D. M.; Brune, R.; Orwar, O.; Jesorka, A. A Multifunctional Pipette. *Lab Chip* **2012**, *12*, 1255.

(43) Ho, J. C. S.; Rangamani, P.; Liedberg, B.; Parikh, A. N. Mixing Water, Transducing Energy, and Shaping Membranes: Autonomously Self-Regulating Giant Vesicles. *Langmuir* **2016**, *32*, 2151−2163.

(44) Gözen, I. Did Solid Surfaces Enable the Origin of Life? *Life* **2021**, *11*, 795.

(45) Bhatia, T.; Agudo-Canalejo, J.; Dimova, R.; Lipowsky, R. Membrane Nanotubes Increase the Robustness of Giant Vesicles. *ACS Nano* **2018**, *12*, 4478−4485.

(46) Vanhille-Campos, C.; Šarić, A. Modelling the Dynamics of Vesicle Reshaping and Scission Under Osmotic Shocks. *Soft Matter* **2021**, *17*, 3798−3806.

(47) Schrum, J. P.; Zhu, T. F.; Szostak, J. W. The Origins of Cellular Life. *Cold Spring Harb Perspect Biol.* **2010**, *2*, a002212−a002212.

(48) Gilbert, W. Origin of Life: The RNA world. *Nature* **1986**, *319*, 618−618.

(49) Saha, R.; Pohorille, A.; Chen, I. A. Molecular Crowding and Early Evolution. *Origins of Life and Evolution of Biospheres* **2014**, *44*, 319−324.

(50) Bridle, H.; Olofsson, J.; Jesorka, A.; Orwar, O. Automated Control of Local Solution Environments in Open-Volume Microfluidics. *Anal. Chem.* **2007**, *79*, 9286−9293.

(51) Schanke, I. J.; Xue, L.; Spustova, K.; Gözen, I. Transport Among Protocells Via Tunneling Nanotubes. *Nanoscale* **2022**, *14*, 10418−10427.

(52) Delamarche, E.; Kaigala, G. V. *Open-Space Microfluidics: Concepts, Implementations, Applications*, 1st ed.; Wiley-VCH: Weinheim, 2018.

(53) Orwick Rydmark, M.; Christensen, M. K.; Köksal, E. S.; Kantarci, I.; Kustanovich, K.; Yantchev, V.; Jesorka, A.; Gözen, I. Styrene Maleic Acid Copolymer Induces Pores in Biomembranes. *Soft Matter* **2019**, *15*, 7934−7944.

(54) Jesorka, A.; Põldsalu, I.; Gözen, I. Microfluidic Technology for Investigation of Protein Function in Single Adherent Cells. *In Methods in Enzymology* **2019**, *628*, 145−172.

(55) Bauer, B.; Davidson, M.; Orwar, O. Direct Reconstitution of Plasma Membrane Lipids and Proteins in Nanotube−Vesicle Networks. *Langmuir* **2006**, *22*, 9329−9332.

(56) Mueller, P.; Chien, T. F.; Rudy, B. Formation and Properties of Cell-Size Lipid Bilayer Vesicles. *Biophys. J.* **1983**, *44*, 375−381.

(57) Gill, S.; Catchpole, R.; Forterre, P. Extracellular Membrane Vesicles in the Three Domains of Life and Beyond. *FEMS Microbiol Rev.* **2019**, *43*, 273−303.

(58) Johansen, J.; Ramanathan, V.; Beh, C. T. Vesicle Trafficking From a Lipid Perspective: Lipid Regulation of Exocytosis in Saccharomyces Cerevisiae. *Cell Logist* **2012**, *2*, 151−160.

(59) Ratajczak, M. Z.; Ratajczak, J. Extracellular Microvesicles/Exosomes: Discovery, Disbelief, Acceptance, and the Future? *Leukemia* **2020**, *34*, 3126−3135.

(60) Wright, P. K.; Jones, S. B.; Ardern, N.; Ward, R.; Clarke, R. B.; Sotgia, F.; Lisanti, M. P.; Landberg, G.; Lamb, R. 17β-estradiol Regulates Giant Vesicle Formation via Estrogen Receptor-Alpha in Human Breast Cancer Cells. *Oncotarget* **2014**, *5*, 3055−3065.

(61) Zhang, D. Y.; Turberfield, A. J.; Yurke, B.; Winfree, E. Engineering Entropy-Driven Reactions and Networks Catalyzed by DNA. *Science (New York, N.Y.)* **2007**, *318*, 1121−5.

(62) Borghi, N.; Kremer, S.; Askovic, V.; Brochard-Wyart, F. Tube Extrusion From Permeabilized Giant Vesicles. *Europhysics Letters (EPL)* **2006**, *75*, 666−672.

(63) Ma, L.; Li, Y.; Peng, J.; Wu, D.; Zhao, X.; Cui, Y.; Chen, L.; Yan, X.; Du, Y.; Yu, L. Discovery of the Migrasome, an Organelle Mediating Release of Cytoplasmic Contents During Cell Migration. *Cell Research* **2015**, *25*, 24−38.

(64) Chattoraj, D. K.; Mitra, A. Adsorption of DNA at Solid−Water Interfaces and DNA−Surfactant Binding Interaction in Aqueous Media. *Curr. Sci.* **2009**, *97* (10), 1430−1438.

(65) Sawant, P. D.; Watson, G. S.; Nicolau, D.; Myhra, S.; Nicolau, D. V. Hierarchy of DNA Immobilization and Hybridization on Poly-L-lysine Using an Atomic Force Microscopy Study. *J. Nanosci. Nanotechnol.* **2005**, *5*, 951−957.

(66) Sharipov, T. I.; Bakhtizin, R. Z. The Estimation of Quantitative Parameters of Oligonucleotides Immobilization On Mica Surface. *IOP Conference Series: Materials Science and Engineering* **2017**, *195*, No. 012002.

(67) Mansy, S. S.; Szostak, J. W. Thermostability of Model Protocell Membranes. *Proc. Natl. Acad. Sci. U. S. A.* **2008**, *105*, 13351−13355.

(68) Tsugane, M.; Suzuki, H. Reverse Transcription Polymerase Chain Reaction in Giant Unilamellar Vesicles. *Sci. Rep.* **2018**, *8*, 9214.

(69) Hindley, J. W.; Elani, Y.; McGilvery, C. M.; Ali, S.; Bevan, C. L.; Law, R. V.; Ces, O. Light-Triggered Enzymatic Reactions in Nested Vesicle Reactors. *Nat. Commun.* **2018**, *9*, 1093.

(70) Zhang, D. Y.; Winfree, E. Control of DNA Strand Displacement Kinetics Using Toehold Exchange. *J. Am. Chem. Soc.* **2009**, *131*, 17303−17314.

(71) Kim, S. C.; Zhou, L.; Zhang, W.; O'Flaherty, D. K.; Rondo-Brovetto, V.; Szostak, J. W. A Model for the Emergence of RNA From a Prebiotically Plausible Mixture of Ribonucleotides, Arabinonucleotides, and 2′-Deoxynucleotides. *J. Am. Chem. Soc.* **2020**, *142*, 2317−2326.

(72) Rao, M.; Eichberg, J.; Oró, J. Synthesis of Phosphatidylcholine Under Possible Primitive Earth Conditions. *Journal of Molecular Evolution* **1982**, *18*, 196−202.

(73) Rao, M.; Eichberg, J.; Oró, J. Synthesis of Phosphatidylethanol-amine Under Possible Primitive Earth Conditions. *Journal of Molecular Evolution* **1987**, *25*, 1−6.

(74) Hargreaves, W. R.; Mulvihill, S. J.; Deamer, D. W. Synthesis of Phospholipids and Membranes in Prebiotic Conditions. *Nature* **1977**, *266*, 78−80.

(75) Liu, L.; Zou, Y.; Bhattacharya, A.; Zhang, D.; Lang, S. Q.; Houk, K. N.; Devaraj, N. K. Enzyme-Free Synthesis of Natural Phospholipids in Water. *Nat. Chem.* **2020**, *12*, 1029−1034.

(76) Toner, J. D.; Catling, D. C. A Carbonate-Rich Lake Solution to the Phosphate Problem of the Origin of Life. *Proc. Natl. Acad. Sci. U.S.A.* **2020**, *117*, 883−888.

(77) Kazmierczak, J.; Kempe, S.; Kremer, B. Calcium in the Early Evolution of Living Systems: A Biohistorical Approach. *Curr. Org. Chem.* **2013**, *17*, 1738−1750.

(78) Hashizume, H. Role of Clay Minerals in Chemical Evolution and the Origins of Life. In *Clay Minerals in Nature*; Intech Open: Croatia, 2012; Vol. *10*, pp 191−208.

(79) Köksal, E. S.; Belletati, P. F.; Reint, G.; Olsson, R.; Leitl, K. D.; Kantarci, I.; Gözen, I. Spontaneous Formation and Rearrangement of Artificial Lipid Nanotube Networks as a Bottom-Up Model for Endoplasmic Reticulum. *JoVE* **2019**, *143*, e58923.

(80) Karlsson, M.; Nolkrantz, K.; Davidson, M. J.; Strömberg, A.; Ryttsén, F.; Åkerman, B.; Orwar, O. Electroinjection of Colloid Particles and Biopolymers Into Single Unilamellar Liposomes and Cells for Bioanalytical Applications. *Anal. Chem.* **2000**, *72*, 5857−5862.

(81) Spustova, K.; Xue, L.; Ryskulov, R.; Jesorka, A.; Gözen, I. Manipulation of Lipid Membranes With Thermal Stimuli. In *Membrane Lipids: Methods and Protocols*; Cranfield, C. G., Ed.; Springer US: New York, NY, 2022; pp 209−225.

(82) Buchholz, T.-O.; Prakash, M.; Krull, A.; Jug, F. DenoiSeg: Joint Denoising and Segmentation. *arXiv*, 2020, arXiv:2005.02987. DOI: 10.48550/arXiv.2005.02987 (accessed November 01, 2022).

(83) Alnæs, M. S.; Blechta, J.; Hake, J.; Johansson, A.; Kehlet, B.; Logg, A.; Richardson, C.; Ring, J.; Rognes, M. E.; Wells, G. N. The FEniCS Project Version 1.5. *Archive of Numerical Software* **2015**, *3*, 9−23.

(84) Spustova, K.; Katke, C.; Villalmanzo, E. P.; Ryskulov, R.; Kaplan, C. N.; Gözen, I. Colony-like Protocell Superstructures. *bioRxiv*, 2021, 2021.09.16.460583. DOI: 10.1101/2021.09.16.460583 (accessed September 04, 2022).